Adaptive Offline Parameter Identification of PMSM With Nonlinear Compensation in Self-Commissioning

Junyu Zhao, Jun Gu, Yuting Wu, *Student Member, IEEE*, and Dianguo Xu, *Fellow, IEEE*

***Abstract*—Accurate offline parameter identification of unknown permanent magnet synchronous machines (PMSMs) without tuned current controllers remains challenging due to nonlinearities and safety constraints. Therefore, this article proposes a hybrid open/closed-loop identification strategy incorporating nonlinear compensation for automated parameter identification. An excitation-adaptive amplitude–frequency open-loop injection scheme is proposed to safely excite unknown PMSMs while eliminating phase-measurement errors in identification, thereby enabling efficient and high-precision open-loop parameter identification. Within a single closed-loop ramp current-injection procedure, simultaneous stator resistance identification and inverter nonlinearity compensation are achieved, enhancing the speed and accuracy of identification. Furthermore, skin-effect compensation is implemented via analysis of mid- and high-frequency current responses to improve inductance-identification precision. The framework uniquely integrates compensation for critical nonlinearities while eliminating manual intervention. Validation on a 750 W PMSM confirms enhanced accuracy, operational efficiency, and reliability.**

***Index Terms*—Inverter nonlinearity, magnetic saturation, parameter identification, permanent magnet synchronous machine (PMSM), skin effect.**

I. Introduction

PERMANENT magnet synchronous machine (PMSM) has gained prominence in various industrial applications due to its superior efficiency, high power density, and robust performance [1], [2], [3], [4], [5]. To attain high-performance motor control, the utilization of motors necessitates complex manual tuning, posing difficulties and inconveniences in the application and hindering the advancement of the industry [6], [7], [8]. Self-commissioning, which involves the automatic setting of control parameters for unfamiliar motors without manual intervention, relies heavily on the precise motor parameters [9], [10], [11]. Consequently, the development of parameter identification strategies that meet the requirements for self-commissioning operation and ensure high generalizability in drive systems has emerged as a significant research gap in the current field.

Researchers have conducted extensive and in-depth studies on the parameter identification of motors to date. Based on the classification of the injected signals, resistance identification algorithms can be divided into time-domain response computation via sinusoidal or step injection [14], two-stage injection to compute the quotient of voltage and current errors [15], and linear regression-based ramp current injection [12], [13], [16]. The identification of inductance parameters of PMSMs can be classified according to the calculation method into using data in the time domain [12], [13], [14], [15], [16], [17], [18] and calculating in the frequency domain [11], [19]. Moreover, from the perspective of the control-loop configuration, existing methods can be categorized into open-loop signal injection methods [11], [12], [13], closed-loop controller-based identification methods [15], [16], [17], [18], [19], and hybrid schemes that combine both approaches [14], [20]. In the event that the current controller has already been tuned, the authors in [15], [16], [17], and [18] implement the inductance identification by obtaining the amplitude and frequency of the response to the injected high-frequency (HF) signal, while the authors in [16] and [18] simultaneously superimpose dc signal to simulate different saturation states of the motor. Besides, the authors in [13] and [20] study the method of flux-linkage identification, from which the inductances can then be derived.

However, the above research lacks consideration of "self-commissioning" and "generalizability." First, it is crucial to acknowledge that the setting of the current closed-loop controller and the rotor position data, in turn, rely on the precise motor parameters. This presents a contradiction in terms of the reciprocal presuppositions of each other [11], [12], [17]. The authors in [21], [22], and [23] provide empirically based methods for adaptive acquisition of controller or position information. However, these methods are quite complex and time-consuming, and therefore do not meet the need for fast self-commissioning. In contrast, the identification strategy of open-loop signal injection appears to be a more reasonable choice. Existing open-loop signal injection methods for PMSM parameter identification often lack adaptive safety mechanisms, risking overcurrent or insufficient excitation under unknown motor conditions [11], [12]. In order to address this problem, Erturk and Akin [12] propose a controlled sinusoidal voltage open-loop injection to estimate

Received 28 July 2025; revised 30 November 2025; accepted 23 December 2025. Date of publication 1 January 2026; date of current version 20 March 2026. This work was supported by the National Natural Science Foundation of China under Grant U22A20217. Recommended for publication by Associate Editor B. K. Lee. *(Corresponding author: Dianguo Xu.)*

The authors are with the School of Electrical Engineering and Automation, Harbin Institute of Technology, Harbin 150001, China (e-mail: 20b906031@stu.hit.edu.cn; 24s006031@stu.hit.edu.cn; wuyuting0711@163.com; xudiang@hit.edu.cn).

Color versions of one or more figures in this article are available at https://doi.org/10.1109/TPEL.2025.3650201.

Digital Object Identifier 10.1109/TPEL.2025.3650201

the spatial inductance map in order to improve the safety and versatility of the identification. Considering the cross-coupling and magnetic saturation effects, the inductances under various operating conditions are obtained by varying the injection amplitude, as described in [13] and [31]. However, their amplitude selection relies on empirical thresholds, and the fixed step-size increment not only fails to achieve a rapid target response but also leads to excessive resource consumption and prolonged time cost. Recently, online parameter identification combined with controller correction has gained popularity in academia as a strategy to address parameter uncertainties [8]. Nevertheless, in practical applications, due to the limited computational power of controllers, online corrections are often completed too late to be effective.

Furthermore, substantial efforts have been made in the existing literature to improve identification accuracy. While advanced adaptive observers (e.g., the leakage-type observer [30], [31]) offer powerful solutions for online disturbance estimation, they are designed for systems with pretuned controllers and are not directly applicable to the offline commissioning of unknown motors. Due to the absence of voltage sensing, inverter nonlinearities result in errors between the actual injected voltage and the commanded voltage. Various works on modeling [16], [24] and identification techniques [13], [14], [20] for inverter voltage errors have been reported. However, current strategies typically necessitate a significant number of signal injections and acquisitions, accompanied by complex compensation algorithms. To improve the simplicity and versatility of self-commissioning, further advancements in error compensation are essential. Moreover, during motor identification and operation, particularly at HFs of injected signals, execution of digital time delays [11], [13] and the skin effect [25], [26] is inevitable. Notably, compensation methods for errors caused by the skin effect in offline parameter identification of PMSMs remain largely unexplored.

To bridge these gaps, this article proposes a novel systematic parameter identification framework with the following contributions.

1) This article shows that using the minimum values of the identified parameters as design references is crucial for safe self-commissioning. These minimum values define the stability boundaries of the drive and provide conservative thresholds for online controller adaptation, thereby preventing instability caused by aggressive or improperly tuned parameters.
2) For open-loop identification, we propose a multipoint amplitude-differential method that uses only magnitude responses, instead of the error-prone phase measurements required by conventional phasor-diagram approaches. Based on this method, an amplitude–frequency adaptive search algorithm automatically selects parameter-agnostic excitation conditions across different motors, and a preliminary current controller with an optimized damping ratio is designed prior to closed-loop identification. This combination removes the need for manual tuning and conservative initial guesses while respecting hardware constraints and ensuring both safety and identification accuracy.
3) For closed-loop identification, we develop an integrated procedure in which ramp-signal injection is used to estimate the inverter nonlinearity model and the stator resistance simultaneously, thereby achieving voltage-error compensation without additional excitation sequences. We further analyze the effects of frequency-dependent resistance (skin effect) and design dedicated midfrequency and HF injection tests for their decoupled identification and compensation, leading to improved inductance-identification accuracy.

The rest of this article is organized as follows. Section II investigates the influence of PMSM parameter variations under different operating conditions and outlines a general identification strategy. Section III presents a high-precision open-loop preliminary identification method based on adaptive voltage injection. Section IV introduces the closed-loop identification strategy under magnetic saturation, including resistance identification, inverter nonlinearity compensation, and skin-effect correction. Section V provides experimental validation of the proposed methods and evaluates their accuracy and effectiveness in a self-commissioning context. Finally, Section VI concludes this article.

II. Analysis of the Effect of PMSM Parameters' Variations Under Different Operating Conditions

This section first analyzes how PMSM parameters vary under different operating conditions and how these variations affect system stability and dynamic performance. Based on these insights, we then derive design guidelines for self-commissioning and formulate the overall offline parameter identification strategy, which defines the roles of the open-loop and closed-loop stages in the proposed framework.

A. PMSM Model Analysis

The electrical model of the PMSM in the *d–q* reference frame is given by the following equation:

$$\begin{bmatrix} u_d \\ u_q \end{bmatrix} = R_s \begin{bmatrix} i_d \\ i_q \end{bmatrix} + \frac{d}{dt} \begin{bmatrix} \psi_d \\ \psi_q \end{bmatrix} + \omega_e \begin{bmatrix} -\psi_q \\ \psi_d \end{bmatrix} \tag{1}$$

where u_{dq} and i_{dq} are the *dq*-axis voltage and current, R_s is the stator resistance, ω_e is the electrical rotational speed, and ψ_{dq} is the *dq*-axis flux linkage. The flux linkage can be expressed $\psi_d = L_{d\mathrm{app}} i_{d+} \psi_f$ and $\psi_q = L_{q\mathrm{app}} i_q$. $L_{d\mathrm{app}}$ and $L_{q\mathrm{app}}$ represent the *dq*-axis apparent inductance. Bringing the flux linkage into the above equation gives

$$\begin{bmatrix} u_d \\ u_q \end{bmatrix} = \begin{bmatrix} L_{d\mathrm{inc}} & 0 \\ 0 & L_{q\mathrm{inc}} \end{bmatrix} \frac{d}{dt} \begin{bmatrix} i_d \\ i_q \end{bmatrix} + \begin{bmatrix} R_s & -\omega_e L_{q\mathrm{app}} \\ \omega_e L_{d\mathrm{app}} & R_s \end{bmatrix} \times \begin{bmatrix} i_d \\ i_q \end{bmatrix} + \begin{bmatrix} 0 \\ \omega_e \psi_f \end{bmatrix} \tag{2}$$

where $L_{dq\mathrm{inc}}$ is the *dq*-axis incremental inductance of PMSM, and ψ_f is the rotor permanent magnet flux linkage. In the linear region preceding the knee point of the magnetization curve, the apparent inductance L_{app} is essentially equivalent to the incremental inductance L_{inc}. However, as magnetic saturation

increases, the discrepancy between them becomes increasingly significant. The relationship between inductance and flux linkage can be expressed as follows [13]:

$$L_{dq\text{inc}} = \frac{d\psi_{dq}}{di_{dq}} = \frac{dL_{dq\text{app}} i_{dq}}{di_{dq}}. \tag{3}$$

As the preliminary step of self-commissioning, it is often essential to model and analyze unknown PMSMs in the stationary frame of reference. The transformation of the dq-axis voltage (2) to the stationary coordinate system is obtained

$$\begin{aligned}\begin{bmatrix} u_\alpha \\ u_\beta \end{bmatrix} = &\begin{bmatrix} L_1 + L_2\cos 2\theta_e & L_2 \sin 2\theta_e \\ L_2 \sin 2\theta_e & L_1 + L_2 \cos 2\theta_e \end{bmatrix} \\ &\times \frac{d}{dt}\begin{bmatrix} i_\alpha \\ i_\beta \end{bmatrix} + \omega_e \psi_f \begin{bmatrix} -\sin\theta_e \\ \cos\theta_e \end{bmatrix} \\ &+ \begin{bmatrix} R_s + \omega_e L_4 \sin 2\theta_e & -\omega_e L_3 + \omega_e L_4 \cos 2\theta_e \\ \omega_e L_3 + \omega_e L_4 \cos 2\theta_e & R_s + \omega_e L_4 \sin 2\theta_e \end{bmatrix} \\ &\times \begin{bmatrix} i_\alpha \\ i_\beta \end{bmatrix} \end{aligned} \tag{4}$$

where the intermediate variables L_{1234} are in the form of inductive combinations

$$\begin{aligned} L_1 &= \left(L_{d\text{inc}} + L_{q\text{inc}}\right)/2 \quad L_2 = \left(L_{d\text{inc}} - L_{q\text{inc}}\right)/2 \\ L_3 &= \left(L_{d\text{app}} + L_{q\text{app}}\right)/2 \quad L_4 = \left(L_{d\text{app}} - L_{q\text{app}}\right)/2. \end{aligned} \tag{5}$$

To achieve the accurate motor control, it is essential to simultaneously determine all motor parameters, including both apparent and incremental inductances. While the full-state incremental inductance surface can be identified, and the apparent inductance can be calculated using (3), this method significantly escalates resource consumption and time costs, contradicting practical application requirements.

B. Analysis of Time-Varying Characteristics of PMSM Parameters

The key factors influencing a motor's resistance are temperature and frequency. In metal conductors, resistance rises with increasing temperatures [15], [25]. Moreover, as frequency increases, current tends to concentrate on the conductor's outer surface, a phenomenon that results in higher resistance, known as the skin effect [25], [26].

The inductance of PMSM is determined by the ratio of the electromagnetic field flux to the current in the equivalent circuit. During motor operation, magnetic saturation effects and cross-coupling phenomena arise due to the properties of the electromagnetic materials. Fig. 1(a) illustrates the relationship between magnetic field strength and the flux density of ferromagnetic materials, where the slope is approximately proportional to the inductance. Fig. 1(b) depicts the finite-element fitting surface of the dq-axis magnetic flux linkage. As the magnetic field strength increases, the degree of magnetic saturation rises, causing the permeability to decrease and subsequently reducing the equivalent inductance. Furthermore, for the IPMSM, the straight-axis magnetic path reluctance is high and the cross-axis magnetic path reluctance is low, resulting in $L_d < L_q$.

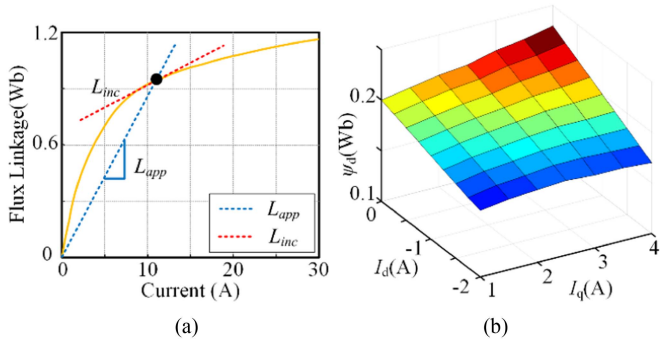

Fig. 1. Time-variant characteristics of inductance. (a) Magnetic saturation: characteristic of the flux and current. (b) Cross coupling: flux linkage under different dq-axis currents.

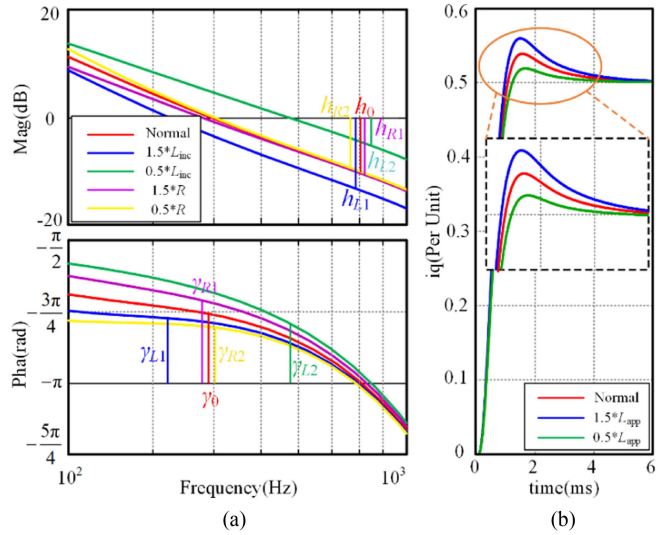

Fig. 2. Time–frequency domain characteristics with distorted parameters. (a) Frequency domain. (b) Time domain.

C. Impact of PMSM Parameter Variations on System Behavior

The initiation of self-commissioning relies on motor parameters identified offline, which form the basis for subsequent controller design. However, being a nonlinear and highly coupled system, the parameters of PMSMs fluctuate due to various influencing factors. Real-time identification under all conditions is resource intensive and impractical for self-commissioning. Instead, a secure identification strategy should prioritize system stability by analyzing parameter variation ranges and their impacts.

To analyze the effect of parameter changes on the system characteristics, Fig. 2 illustrates the fluctuations in system behavior within the time or frequency domain caused by parameter changes. The pink and yellow curves in Fig. 2(a) depict the system characteristics after changes in resistance. Upon stator resistance augmentation, stable margins exhibit a positive trend, suggesting a positive correlation among temperature, frequency, and system stability. The blue and green curves in Fig. 2(a) represent the system characteristics following incremental inductance variations. While phase margins (γ_{L1} and γ_{L2}) remain

relatively unaffected, reduced inductance significantly lowers the gain margin h_{L2}, raising the risk of instability. Apparent inductance directly influences feedforward compensation for back electromotive force (EMF): compensation leads to greater overshoot and longer settling time, whereas a lower value mitigates or eliminates overshoot at the expense of a slightly slower response. Fig. 2(b) presents the time-domain effects of varying feedforward levels, with minimal feedforward generally favored in practice to maintain stability.

In addition to stability margins, the impact of parameter mismatches on current control bandwidth is a critical yet often overlooked aspect in high-performance drive systems. By analyzing the sensitivity of the current-loop model, it can be concluded that resistance mismatch mainly affects steady-state error and low-frequency characteristics, with limited impact on bandwidth. Inductance mismatch directly influences the dynamic response of the current loop, and underestimating inductance during controller design results in lower actual bandwidth and slower responses. Back EMF mismatch, particularly at higher speeds, reduces the effective control voltage available for the current loop, indirectly decreasing system bandwidth. These observations underscore the importance of identifying the minimum inductance during self-commissioning to establish reliable design baselines, thereby preventing bandwidth and dynamic deterioration caused by parametric underestimation.

Based on the above analysis, the parameter variations of PMSMs mainly affect the stability margins, bandwidth, and dynamic performance of the current loop, and identifying the minimum inductance values is crucial for guaranteeing conservative yet stable controller design. Therefore, instead of attempting real-time identification under all operating conditions, this article adopts a two-stage offline strategy for self-commissioning. The system employs an open-loop stage to safely identify the apparent resistance and inductance and provide initial controller tuning, followed by a closed-loop stage that precisely refines the incremental inductance under magnetic saturation. The overall architecture of the proposed parameter identification framework is summarized in Fig. 8, and the corresponding α-axis current and voltage waveforms over the entire process are shown in Fig. 9, where the open-loop and closed-loop stages are highlighted in different shaded regions. In the proposed offline self-commissioning process, all current-injection stages are completed within only a few seconds. Because the duration is extremely short, the stator winding temperature remains effectively constant, and the temperature-induced variation of stator resistance is negligible.

III. High-Precision Open-Loop Preliminary Identification With Adaptive Injection

In the first stage of the proposed framework (orange region in Fig. 9), an open-loop identification procedure is carried out before any current controller is tuned. The objective of this section is to safely and efficiently identify the apparent resistance and inductance of the unknown PMSM and to provide initial current-loop controller parameters for subsequent closed-loop identification.

A. Identification of Apparent Impedance Through Variable Amplitude–Frequency Signal Injection

In the case of open-loop fixed vector angular injection, Maxwell's force directs the motor rotor toward a designated EMF vector. At this point, (4) can be simplified to

$$\begin{bmatrix} u_a \\ u_\beta \end{bmatrix} = \begin{bmatrix} L_1 + L_2\cos 2\theta_e & L_2 \sin 2\theta_e \\ L_2 \sin 2\theta_e & L_1 + L_2\cos 2\theta_e \end{bmatrix} \frac{d}{dt} \begin{bmatrix} i_a \\ i_\beta \end{bmatrix} + R_s \begin{bmatrix} i_a \\ i_\beta \end{bmatrix}. \tag{6}$$

When the injection vector angle equals zero, the above equation can be further simplified as follows:

$$u_\alpha = R_s i_\alpha + L_{\alpha\mathrm{inc}} \frac{d}{dt} i_\alpha. \tag{7}$$

The response of the PMSMs equivalent impedance model can be expressed as follows when the injected sinusoidal voltage signal is $U_m e^{j(\omega t+\theta u)}$:

$$U_m e^{j(\omega t+\theta_u)} = R_s I_m e^{j(\omega t+\theta_i)} + \omega I_m L_{\alpha\mathrm{app}} e^{j(\omega t+\theta_i+\pi/2)}. \tag{8}$$

Since the current varies over a wide range at this point, it is expressed in the standard form of inductance L_d rather than as incremental inductance $L_{d\mathrm{inc}}$. From the above equation, L_d and R_s can be expressed as follows [11], [18]:

$$L_{\alpha\mathrm{app}} = \frac{U_m}{\omega I_m} \sin(\theta_u - \theta_i) \tag{9}$$

$$R_s = \frac{U_m}{I_m} \cos(\theta_u - \theta_i) \tag{10}$$

where U_m, I_m, θ_u, θ_i, and ω represent the amplitude, phase angles, and frequency of the input voltage and current response, respectively. However, the actual signal injection process is constrained by several nonlinear factors. First, the inverter's nonlinearity introduces additional resistive characteristics to the system, reducing the actual applied voltage below the commanded level and adversely affecting the identification results. Second, the inherent discretization in digital control inevitably introduces errors in the acquired signals. Specifically, the impedance phase angle is calculated as $\theta_u - \theta_i = \omega(t_i - t_u)$, where t_i and t_u represent the zero-crossing instants of the voltage and current, respectively.

The accuracy of this calculation is intimately tied to the sampling rate f_s, and the phase calculation error can be expressed as follows:

$$E = \theta_e - \theta_e{}' = \arctan\left(\frac{\omega L_{\alpha\mathrm{app}}}{R}\right) - \omega\Delta t \tag{11}$$

where the error source Δt is obtained from the time difference between the voltage command and the current sample, often calculated by measuring the instant at which the current signal intersects zero. The value can, thus, be upwardly rounded to the nearest integer multiple of the sampling frequency, which is expressed when the response is stable and error free

$$\Delta t = \left\lceil \frac{\theta_e}{\omega} f_s \right\rceil / f_s = \left\lceil \frac{\arctan(\omega L_{\alpha\mathrm{app}}/R)}{\omega} f_s \right\rceil / f_s. \tag{12}$$

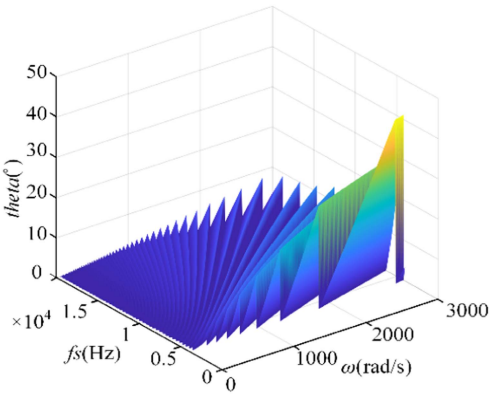

Fig. 3. Phase sampling error under different operating states.

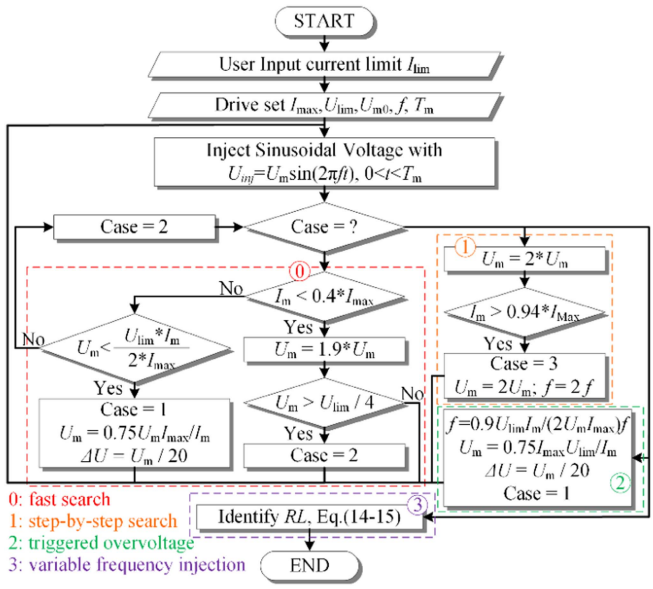

Fig. 4. Flowchart of an automated voltage injection strategy.

According to the engineering experience, the injection signal frequency ω is set within the interval [0, 3000] rad/s, and the sampling frequency f_s ranges from 4000 to 20 000 Hz. In addition, the motor's electrical time constant $L/R = 2.5{*}10^{-3}$ s. A 3-D plot depicting the parameter identification error is shown in Fig. 3. The sample error significantly surges when ω decreases and f_s escalates. To achieve high-precision parameter identification, the parameters involved in computation should be minimally affected by sampling noise or external interference. Given the inherently lower relative amplitude fluctuation ($\Delta A/A_{\max}$) in the amplitude of response signals, a multipoint amplitude-differential technique is developed. This method exclusively employs response amplitudes at discrete frequencies for motor parameter identification, ensuring superior quantification accuracy.

Taking the sum of the squares of (9) and (10) results in

$$U_m^2/I_m^2 = \omega^2 L_{\alpha\text{app}}^2 + R_s^2. \tag{13}$$

The inductance is calculated by subtracting the two sets of variable-frequency data, and the result is given as follows:

$$L_{\alpha\text{app}} = \sqrt{\frac{(U_2/I_2)^2 - (U_1/I_1)^2}{\omega_2^2 - \omega_1^2}}. \tag{14}$$

For the inductance identification in (14), two operating points at different excitation frequencies are required. Because the inductance depends on the degree of magnetic saturation, the two similar operating conditions should be selected such that the resulting current amplitudes are as close as practically achievable. Ideally, when the dc bus voltage has sufficient headroom, both the injection frequency and the voltage amplitude are doubled so that the current amplitude remains nearly unchanged, as illustrated in Fig. 5(a).

Using previously derived inductance from (14), the resistance can be calculated as follows:

$$R_s = \sqrt{\frac{U_3^2 - U_1^2}{I_3^2 - I_1^2} - \omega^2 L^2}. \tag{15}$$

The open-loop identification strategy proposed in this section is implemented by combining reliable parameters for different operating conditions. Nevertheless, it necessitates precise specifications for the amplitude and frequency of the injected voltage. Hence, in Section III-B, an algorithm is designed to automatically search for the amplitude and frequency of the injected signal in line with practical application requirements.

B. Adaptive Amplitude–Frequency Search Algorithm for Signal Injection

The identification strategy must be conducted under suitable amplitude–frequency operating conditions. Apart from ensuring the effectiveness and safety of the identification, the self-commissioning identification algorithm developed in this article aims to achieve the quickest possible open-loop injection and minimum inductance identification at maximum current through an adaptive search strategy. Therefore, integrating the previously designed multipoint amplitude-differential identification, an amplitude–frequency adaptive search algorithm is developed. The detailed implementation procedure of this strategy is illustrated in Fig. 4.

In unknown electromechanical systems, minimizing user input parameters enhances strategy intelligence and reduces the risk of misconfiguration. The proposed strategy requires setting a current limit I_{lim}. This limit is determined by the constraints of the drive and motor, along with operational requirements, to avoid excessive copper loss and guarantee safe offline operation. As for the initialization settings of other parameters, bus voltage U_N can be obtained by sampling, and the initial injection amplitude U_{m0} can be set at twice the inverter voltage drop. For identification validity, the initial injected signal frequency f_0 is chosen far above the switching frequency and near the electrical time constant's reciprocal. Therefore, the smaller value between one-tenth of the switching frequency and 100 Hz is used in this article. In addition, to minimize errors due to signal transient response fluctuations, the period T_m is set to $4/f_0$ (s).

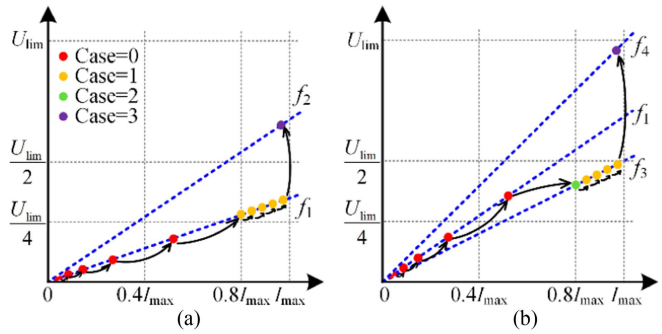

Fig. 5. Examples of process state diagram for automatic injection selection. (a) No voltage protection trig. (b) Voltage protection trig.

After completing the initial injection, the amplitude and frequency of the injection signal should be gradually increased to meet the desired identification conditions. The injected signal amplitude U_m exponentially doubles until the response current amplitude I_m exceeds $0.4{*}I_{\max}$, approaching the recognition threshold. Subsequently, exiting the fast search phase, the subsequent voltage injection amplitude is calculated as follows:

$$U_m = 0.8 \times U_m \times I_{\max}/I_m. \tag{16}$$

To obtain the required data for resistance identification as per (15), the injected signal is progressively augmented in increments of ΔU [1/20 of (16)], until the response current amplitude I_m exceeds $0.94{*}I_{\max}$. For inductive discrimination as per (14), the frequency of the voltage command is doubled and reinjected. This action almost doubles the impedance of the controlled object. Thus, to maintain the same level of magnetic saturation for identifying working conditions, the command amplitude must also be doubled.

The actual voltage injection process is constrained by the bus voltage, especially in conditions characterized by low bus voltage and high inductance. $U_{\lim}$ is chosen as the inverter's maximum fundamental output phase voltage within the linear modulation range, which is $0.577{*}U_N$. Considering the margin required for the final variable-frequency injection, the threshold voltage is set as $U_{\lim}/2$ during open-loop iterative injection, and the voltage state is predicted in real time during the injection process. If the threshold voltage is about to be exceeded, adjust the amplitude and frequency of the injected signal accordingly.

Fig. 5 shows a state diagram illustrating the injection process described above. Specifically, in Fig. 5(a), the system goes through three sequential stages: fast search, step-by-step search, and variable-frequency injection, completing the safe injection process. Conversely, Fig. 5(b) highlights a scenario where the voltage protection threshold $V_{\lim}$ is activated prior to achieving $I_{\max}$, attributable to higher motor impedance and/or lower bus voltage. When the dc bus-voltage constraint becomes active, the direct "double-frequency and double-amplitude" rule would exceed the voltage limit before the current can reach the desired amplitude. Therefore, the algorithm first decreases the excitation frequency to f_3 so that the current can still approach the high-current region under the bus-voltage limit. After the current reaches the target amplitude, the excitation frequency and amplitude are adjusted to f_4, providing the second measurement point required by (14). In this manner, the two impedance measurements satisfy both the voltage and current constraints while keeping the current amplitudes as close as practically achievable.

C. Optimal Damping Ratio-Based Design Method for Current-Loop Controllers

For achieving subsequent closed-loop injection and identification, a model-based controller tuning method is used once the apparent parameters have been identified. In the stationary state of the PMSM, the open-loop transfer function of the system is formulated as follows:

$$G_{\mathrm{OL}} = G_{\mathrm{PI}} G_M G_d = \frac{k_p k_i}{Rs} \frac{\tau_i s + 1}{\tau_e s + 1} e^{-sTd} \tag{17}$$

where k_p [V/A] and k_i [1/s] are the proportional and integrator gain, respectively, and time constant τ_i is the reciprocal of k_i, and motor time constant τ_e equals L_d/R. T_d represents the time delay of system.

To facilitate the derivation, the modulation and transfer delay $G_d(s)$ can be approximated by the second-order Padé expansion as follows:

$$G_d = e^{-sTd} \approx \frac{1 - sT_d/2 + s^2T_d^2/12}{1 + sT_d/2 + s^2T_d^2/12}. \tag{18}$$

Based on engineering experience, τ_i is often chosen to be equal to avoid the effect of dominant poles. By substituting (18) into (17), the characteristic equation of the system is given as follows:

$$\frac{LT_d^2}{12}s^3 + \frac{k_pT_d^2 + 6LT_d}{12}s^2 + \frac{2L - k_pT_d}{2}s + k_p = 0. \tag{19}$$

The damping ratio is often set at 0.707 in control system design, striking an optimal equilibrium between fast response and minimized oscillation. To achieve this design goal, consider the characteristic equation's roots in the form of $s = -a \pm aj$, the real and imaginary parts of the characteristic equation are, respectively, as follows:

$$\begin{aligned} &\frac{LT_d^2a^3}{6} - aL + \frac{k_pT_da}{2} + k_p = 0 \\ &\frac{LT_d^2a^3}{6} - \frac{k_pT_d^2a^2}{6} - LT_da^2 + aL - \frac{k_pT_da}{2} = 0. \end{aligned} \tag{20}$$

Treating the variables a and k_p as unknowns, solving the above binary equation gives (irrational values are discarded)

$$k_p = 0.5054L/T_d. \tag{21}$$

Obviously, the controller parameters designed here are between the maximum gain method [29] and the minimum overshoot method [27], which are also reasonable and instructive.

This section addresses the signal error issues and adaptive safety injection strategies in open-loop identification. The parameters identified here, R_{sopen} and $L_{\alpha\mathrm{app}}$, not only facilitate initial controller tuning but also establish a benchmark for subsequent closed-loop results, thereby embedding a layer of cross validation throughout the process. Section IV will discuss the challenges associated with closed-loop identification.

IV. Highly Accurate Identification of Maximum Magnetic Saturation Inductance

After the open-loop stage in Section III has provided apparent parameters and an initial current controller, the second stage of the proposed framework performs high-precision closed-loop identification under magnetic saturation (blue, yellow, and purple regions in Fig. 9). As outlined in the blue block of Fig. 8, the procedure first identifies the stator resistance and inverter nonlinearity via ramp current injection, and then performs HF voltage injection at saturated operating points to discriminate the incremental inductance. Section IV-A details the resistance identification with inverter nonlinearity compensation, whereas Section IV-B details the analysis of skin-effect-induced errors and proposes a vector-projection-based compensation method, enabling the accurate inductance identification under magnetic saturation.

A. Stator Resistance Identification With Inverter Nonlinearities Compensation

The stator resistance R_s is identified using ramp current injection in the α-axis, with gradually increasing amplitude. In parallel, the inverter nonlinearity model is identified and compensated to mitigate the voltage error caused by the inverter's dynamic behavior during the identification process. Simultaneously identifying R_s and inverter nonlinearity can shorten the identification process, avoid the influence of temperature drift on resistance values, and ensure that the subsequent closed-loop identification stage starts with minimal error.

The nonideal characteristics of the inverter introduce errors in the resistance identification process, which includes other nonlinear characteristics, such as tube ON-state voltage drop, deadband, and parasitic capacitance [13], [14], [20]. The HF equivalent resistance was introduced in [16] and [24] to present a more accurate voltage-error model. As described in the literature [16], [24], the voltage error of the fundamental wave component can be expressed as follows:

$$\Delta u_{x\mathrm{err}} = 2\Delta U\left(\frac{1}{1+e^{-kix}}-\frac{1}{2}\right)\in[-\Delta U,\Delta U] \tag{22}$$

where x is the three-phase *UVW*, $\Delta u_{x\mathrm{err}}$ is the voltage error due to inverter nonlinearity, i_x is the three-phase fundamental current, ΔU is the saturation value of the voltage error, and k is a model parameter determined only by deadtime and tube characteristics.

The expression for the voltage error in the dq-axis system is derived through coordinate transformation

$$\begin{cases}\Delta u_{d\mathrm{err}} = \frac{2}{3}\left[u_{a\mathrm{err}}\cos\theta_e + u_{b\mathrm{err}}\cos(\theta_e-\frac{2\pi}{3})\right.\\ \qquad\left.+u_{c\mathrm{err}}\cos(\theta_e+\frac{2\pi}{3})\right]\\ \Delta u_{q\mathrm{err}} = -\frac{2}{3}\left[u_{a\mathrm{err}}\cos\theta_e + u_{b\mathrm{err}}\cos(\theta_e-\frac{2\pi}{3})\right.\\ \qquad\left.+u_{c\mathrm{err}}\cos(\theta_e+\frac{2\pi}{3})\right].\end{cases} \tag{23}$$

In the described case of resistive discrimination, once steady state is reached, only the resistive component of the voltage equation remains, where $\theta_e = 0$ and $I_\alpha = I_d \approx I_a \approx -0.5*I_b \approx -0.5*I_c$. Combined with the $\alpha\beta$-axis voltage equation, the above equation can be simplified as follows:

$$u_\alpha = R_s i_\alpha + \Delta u_{d\mathrm{err}}(0^\circ) \tag{24}$$

$$\begin{aligned}\Delta u_{d\mathrm{err}}(0^\circ) &= \frac{2}{3}\left(u_{a\mathrm{err}}(i_a)-\frac{1}{2}u_{b\mathrm{err}}(i_b)-\frac{1}{2}u_{c\mathrm{err}}(i_c)\right)\\ &= \frac{4}{3}\Delta U\left(\frac{1}{1+e^{-ki_\alpha}}-\frac{1}{1+e^{ki_\alpha/2}}\right)\\ &= \frac{4}{3}\Delta U\left(\frac{e^{ki_\alpha/2}-e^{-ki_\alpha}}{\left(1+e^{-ki_\alpha}\right)\left(1+e^{ki_\alpha/2}\right)}\right).\end{aligned} \tag{25}$$

The initial value of ΔU can be calculated by multiplying the bus voltage U_{dc} and the deadtime. However, during the actual switching process of the inverter, the turn-ON time is shorter than the turn-OFF time. As a result, the actual equivalent deadtime is slightly less than the set deadtime. In this article, R_s and ΔU are determined by linearly fitting the voltage–current characteristics. From (25), the slope of the fit is R_s, and the intercept is the maximum value of the voltage error in the d-axis, 4/3$*\Delta U$. To solve for the unknown k in the above equation, it is assumed here that the intermediate variable $x = e^{kid/2}$. The rearranged equation is given as follows:

$$\frac{x^3-1}{x^3+x^2+x+1} = \frac{3}{4}\frac{\Delta u_{d\mathrm{err}}(0^\circ)}{\Delta U} = \Delta U_x \tag{26}$$

where ΔU_x is a new intermediate variable for easy calculation and derivation. From the above equation, the solution of the inverter deadband model at this point can be transformed into a 1-D three-equation solution problem, as follows:

$$(\Delta U_x-1)x^3 + \Delta U_x x^2 + \Delta U_x x + (\Delta U_x+1) = 0. \tag{27}$$

The Shengjin formula can be used to solve the problem, and its discriminant can be simplified as follows:

$$\Delta = B^2 - 4AC = 48\Delta U_x^4 - 108\Delta U_x^2 + 81. \tag{28}$$

Since $\Delta U_x \in [0, 1]$, this discriminant Δ is positive, at which point there exists a unique positive real solution to (27) with the expression

$$x = \frac{-\Delta U_x - \left(\sqrt[3]{Y_1}+\sqrt[3]{Y_2}\right)}{3\left(\Delta U_x-1\right)} \tag{29}$$

where $Y1$ and $Y2$ are the set of intermediate variables, expressed as follows:

$$\begin{aligned}Y_{1,2} &= 10\Delta u_x^3 - 9\Delta u_x^2 - 13.5\Delta u_x\\ &\quad + 13.5 \pm 1.5\left(\Delta u_x - 1\right)\sqrt{\Delta}.\end{aligned} \tag{30}$$

The results of (29) are logarithmically transformed and the model parameter k is calculated as follows:

$$k = 2\mathrm{In}x/i_\alpha. \tag{31}$$

The calculated parameter k is an array of one-to-one correspondence with the current i_α. The accuracy of the model's fit to the voltage equation can be evaluated before proceeding with further iterations of the model parameters. After obtaining the model parameter, in order to further simplify inverter compensation, (23) can be calculated by fitting a high-order

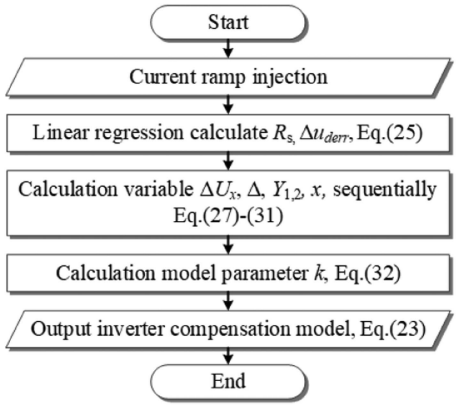

Fig. 6. Flowchart of the stator resistance estimation with inverter nonlinearities compensation.

polynomial. Fig. 6 outlines the designed inverter nonlinear identification process, which is implemented in the preliminary stage of closed-loop identification, i.e., the first blue region in Fig. 9.

Through the above series of derivations, this section proposes a method that simultaneously achieves resistance identification and compensation of inverter nonlinearities in a very short time without additional injections. The complexity of the algorithm is reduced by transforming the inverter nonlinearity detection problem into solving for the model parameters. The compensation can be achieved through polynomial fitting calculations, which avoids the traditional complexity of measuring and compensating for different voltage angle conditions one by one using lookup tables. This method is simple and efficient, meeting the needs of self-commissioning and parameter identification with fast and strong adaptability.

B. Analysis of the Influence of HF Skin Effect and Compensation Method

When the motor operates in the magnetic saturation region and HF voltage injection is applied, the skin effect causes the HF current to crowd near the conductor surface, which significantly increases the effective ac resistance R_{skin}. As a result, the apparent resistance in the identification model becomes R_{skin}, whereas the incremental inductance remains the quantity of interest. If this frequency-dependent resistance is ignored, the inductance computed from the α-axis equivalent model will be systematically overestimated.

From the α-axis voltage equation in (7), the ideal HF relationship between the injected voltage and current can be written as follows:

$$u_{\alpha h} = R_s i_{\alpha h} + j\omega_h L_{\alpha\mathrm{inc}} i_{\alpha h} \tag{32}$$

where $u_{\alpha h}$ and $i_{\alpha h}$ are the complex phasors of the injected HF voltage and current at angular frequency ω_h. In this ideal case, the resistive voltage component is strictly in phase with the current, while the inductive component is exactly in quadrature. Accordingly, the incremental inductance can be obtained as follows:

$$L_{\alpha\mathrm{inc}} = \frac{\mathrm{Im}\left\{u_{\alpha h}\right\}}{\omega_h \left|i_{\alpha h}\right|} = \frac{\left|u_{\alpha h}\right| - R_s \left|i_{\alpha h}\right|}{\omega \left|i_{\alpha h}\right|}. \tag{33}$$

However, in practice, two major nonidealities distort this relationship. System delay (including pulsewidth modulation, computation, and sampling delays) introduces an additional phase lag between the commanded voltage and the measured current, rotating phasors by $\omega_h T_d$. Besides, skin effect increases the in-phase resistive component R_{skin}, which changes the magnitude and phase of the total voltage without altering the true inductive component. If one simply substitutes the measured amplitudes $u_{\alpha h}$ and $i_{\alpha h}$ into (33) while assuming a constant resistance R_s, both effects combine to yield an inductance larger than the true $L_{\alpha\mathrm{inc}}$.

To address this problem, we propose a two-stage compensation strategy based on delay identification and vector projection, as illustrated by the yellow and purple regions in Fig. 9.

First, the phase lag caused by the total system delay T_d is identified and removed so that the remaining phase difference reflects only the electrical impedance characteristics. A chirp signal with fixed current amplitude and sweep frequency up to $f_s/2$ is injected in the α-axis, and the complex voltage–current ratio is obtained by fast Fourier transform (FFT) at each frequency. $\theta_{\mathrm{FFT}}(\omega)$ denotes the measured phase angle between voltage and current, and let the ideal delay-free phase be

$$\theta_{\mathrm{ideal}}(\omega) = \arctan\left(\frac{\omega L_{\alpha\mathrm{inc}}}{R_s}\right). \tag{34}$$

At sufficiently HF ($\omega \gg 1/\tau_e$), the phase of the motor system remains virtually constant at $-\pi/2$. Thus, the total delay T_d can be derived by fitting the additional phase lag in this HF range as follows:

$$T_d = \frac{\theta_{\mathrm{FFT}}(\omega) - \theta_{\mathrm{ideal}}(\omega)}{\omega} \approx \frac{\theta_{\mathrm{FFT}}(\omega) + \pi/2}{\omega}. \tag{35}$$

Using the identified T_d, the measured phase at any frequency can be corrected to remove the delay effect

$$\theta_{\mathrm{corr}}(\omega) = \theta_{\mathrm{FFT}}(\omega) + \omega T_d. \tag{36}$$

This step establishes a baseline for distinguishing between delay-induced phase lag and skin-effect distortion.

Second, after delay compensation, the HF voltage–current relationship at the identification frequency ω_h can be expressed as follows:

$$u_{\alpha h}(\omega_h) = R_{\mathrm{skin}}(\omega_h) i_{\alpha h}(\omega_h) + j\omega_h L_{\alpha\mathrm{inc}} i_{\alpha h}(\omega_h). \tag{37}$$

Let $|U_{\mathrm{FFT}}|$ and θ_{corr} denote the magnitude and delay-corrected phase angle of the voltage phasor with respect to the current phasor obtained from FFT at frequency ω_h. We choose the current phasor as the real axis so that the in-phase component of the voltage corresponds to the total resistive drop, affected by R_{skin}, and the quadrature component corresponds to the purely inductive drop, independent of R_{skin}. The quadrature component of the delay-corrected voltage is then obtained by projecting the voltage vector onto the axis perpendicular to the current vector

$$U_{\mathrm{qua}} = |U_{\mathrm{FFT}}| \cos(\theta_{\mathrm{corr}} + \pi/2) = |U_{\mathrm{FFT}}| \sin(\theta_{\mathrm{corr}}). \tag{38}$$

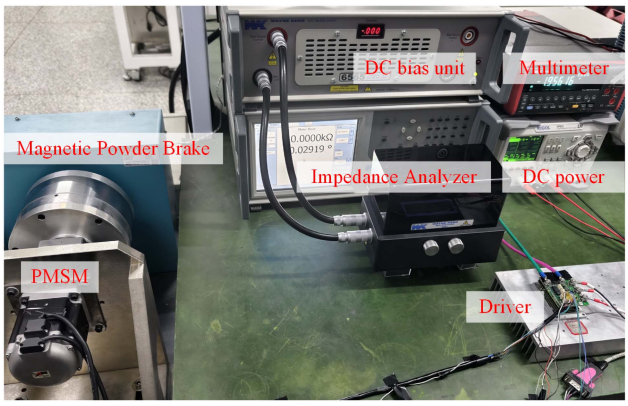

Fig. 7. Hardware experimental platform.

TABLE I
MAIN PARAMETERS OF THE SYSTEM

Symbol	Parameter	Value
P_N	Motor Power	750W
I_N	Nominal Current	7.07A
t_{dead}	deadtime	3.2μs
ψ_f	flux linkage	0.056Wb
T_N	Nominal Torque	2.39N·m

Since U_{qua} corresponds to $\omega_h L_{\alpha\mathrm{inc}}|i_{\alpha h}|$, the incremental inductance $L_{\alpha\mathrm{inc}}$ under magnetic saturation can finally be computed as

$$L_{\alpha\mathrm{inc}} = \frac{U_{\mathrm{qua}}}{\omega_h\,|i_{\alpha h}|} = \frac{|U_{\mathrm{FFT}}|\sin(\theta_{\mathrm{corr}})}{\omega\,|i_{\alpha h}|}. \tag{39}$$

By rotating the voltage–current phasor pair to remove the delay-induced phase lag and then projecting the compensated voltage vector onto the direction orthogonal to the current, the identification algorithm effectively discards all contributions from the unknown, frequency-dependent resistive term. The resulting inductance estimate depends solely on the quadrature component and, thus, remains insensitive to skin effect. This two-stage procedure provides a simple yet robust way to isolate the true inductive component under HF excitation. The inductance $L_{\alpha,\mathrm{inc}}$ obtained here represents the incremental inductance under dc-biased magnetic saturation, whereas the earlier open-loop identified $L_{\alpha,\mathrm{app}}$ corresponds to the apparent inductance. Their consistent relationship provides an additional stagewise validation of the proposed framework, as demonstrated in Section V-D.

V. EXPERIMENTAL RESULTS

In order to test the effectiveness of the offline parameter identification algorithm studied in this article and its versatility in self-commissioning applications, an experimental validation and testing platform was built, as shown in Fig. 7. The motor under test in the platform is a 750 W TAMAGAWA TS4614N7680 servo motor. A magnetic particle brake is used as the load. Detailed parameters of the drive system and controller are presented in Table I.

To ensure the credibility of the performance evaluation of the proposed offline identification algorithm, high-precision reference ground-truth values for the motor parameters were established through metrology-grade measurements and rigorously controlled test procedures. A comprehensive test platform integrating all measurement instruments and the motor under test was constructed. The stator dc resistance was measured using a $5\frac{1}{2}$-digit UNI-T UT805 digital multimeter (0.001-Ω resolution and $\pm 0.08\% + 50$ accuracy) in a four-wire Kelvin configuration, effectively eliminating the influence of lead and contact resistance. To verify that the winding temperature remained nearly constant during the proposed identification, a thermal imager FOTRIC 368C monitored the motor casing near the end-winding region and the stator terminal leads. No observable temperature increase was detected during identification, so the temperature effect on the identified stator resistance can be regarded as negligible. The inductance characteristics were obtained using a Wayne Kerr 6500 impedance analyzer, equipped with the Wayne Kerr 6565 10 A dc-bias unit. A small-signal ac excitation was superimposed on the various levels of dc-bias current to measure the impedance, thereby directly acquiring the incremental inductance at specific operating points, effectively replicating the magnetic saturation state of the motor during actual operation. By selecting specialized instruments tailored to each parameter type and by performing measurements under the same operating conditions as those used in the identification experiments, the resulting reference values form a reliable and accurate benchmark for evaluating the proposed method.

The entire parameter estimation process is meticulously designed and comprises three key components: adaptive amplitude–frequency injection with sampling error compensation in open-loop conditions, controller design with optimal damping ratio, and high-precision identification under closed-loop control that accounts for inverter nonlinearities, time delays, and skin effect, as illustrated in Fig. 8. Throughout the standstill identification experiments, the rotor remained effectively stationary. This is attributed to the injection of a substantial α-axis current, thereby creating a powerful "magnetic lock" that anchors the rotor position. The α-axis current and voltage profiles throughout the identification process are shown in Fig. 9, accompanied by an algorithmic overview of each stage, color coded for clarity. Key identification parameters are annotated at their respective phases, illustrating the sequential refinement and validation embedded in the methodology. Crucially, as the process involves a series of parameter identifications, as opposed to a single identification step, the framework is designed to achieve progressive improvement and internal consistency checks. As summarized in Table II, which provides a qualitative comparison between our scheme and existing approaches, it can be readily observed that the proposed method demonstrates significant advantages over previously reported works.

A. Open-Loop Identification With Adaptive Amplitude–Frequency Injection

As established in Section III, the proposed open-loop stage combines a multipoint amplitude-differential identification

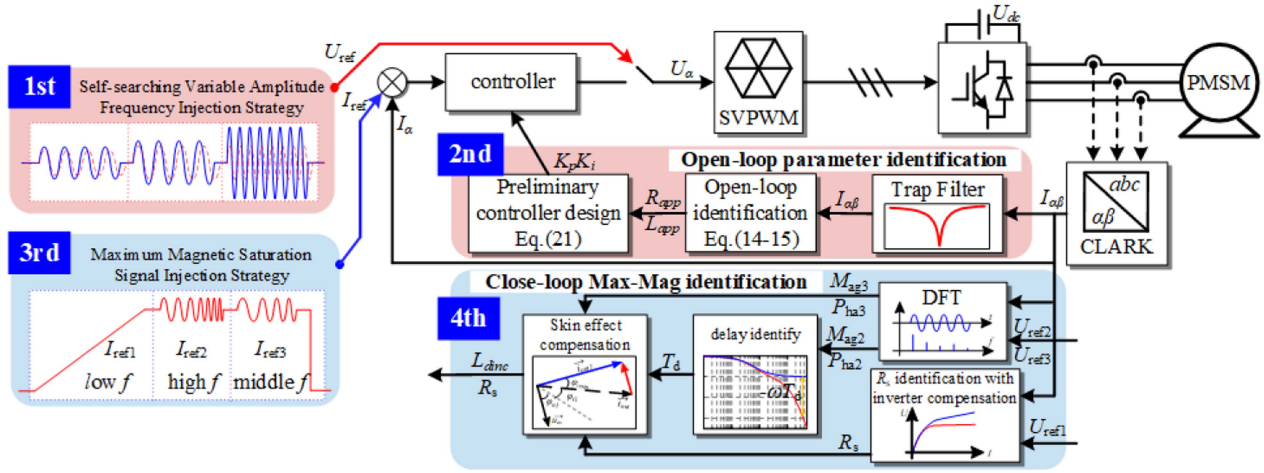

Fig. 8. Overall algorithmic architecture for system parameter identification.

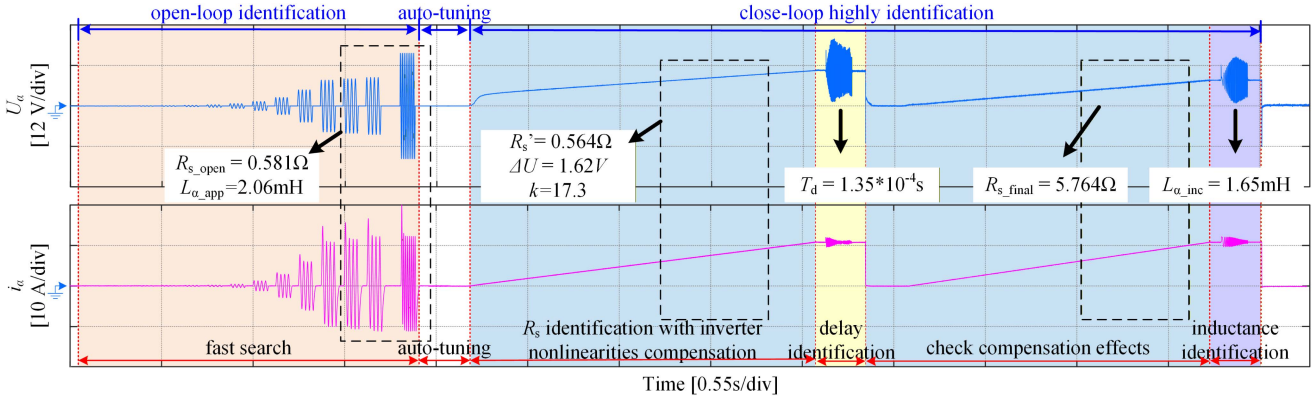

Fig. 9. α-axis current and voltage of the whole identification process.

TABLE II
FEATURE COMPARISON OF THE PROPOSED SCHEME WITH EXISTING METHODS

Method			Identified Parameter		Non-ideal Features Considered				
Control Mode	Technical Proposal	Reference	Incremental inductance	Apparent inductance	Magnetic Saturation	Inverter Nonlinearity	Time Delay	Sampling Error	Skin Effect
Open Loop	Sinusoidal Voltage Injection	[11] [12]		√	√	√	√		
	Square Voltage Test	[13][20]		√	√	√			
	Response Signal Spectral Analysis	[19]	√		√	√			
Close Loop	Time constant calculate	[14]		√		√			
	Est. via phasor diagram	[15]	√		√	√			
	DC-biased AC	[16]-[18]	√		√	√			
	Frequency analysis	[21]	√		√				
Proposed Method	Hybrid Scheme	_	√	√	√	√	√	√	√

method with an amplitude–frequency adaptive search algorithm, enabling the automatic selection of safe and effective injection conditions across different motors without manual tuning. In this section, the behavior and robustness of this adaptive mechanism are experimentally verified.

The experimental waveforms of the open-loop adaptive injection are shown in Fig. 10. Two representative operating conditions are tested to evaluate the universality of the algorithm, a 50-V dc bus with a 7-A current limit, and a more constrained 30-V dc bus with a 10-A current limit. In case (a), the injection voltage undergoes exponential amplitude escalation, stepwise refinement, and variable-frequency excitation. Throughout the process, the predictive overvoltage constraints are never activated, and the response current smoothly reaches $I_{\max}$, confirming that the search strategy can fully utilize the available voltage margin while maintaining safe operation. In case (b), the system operates under stricter voltage constraints. As shown in Fig. 10(b), once the algorithm predicts a potential overvoltage risk from the response characteristics, the subsequent injection amplitude and frequency are automatically adjusted in real time.

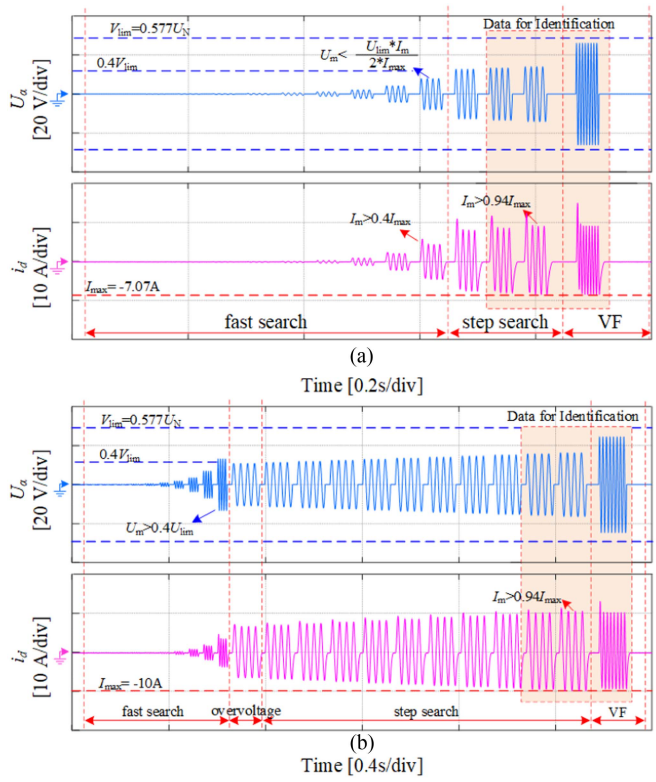

Fig. 10. α-axis current and voltage of open-loop adaptive injection. (a) Sufficient DC-bus voltage without triggering overvoltage prediction. (b) Limited DC-bus voltage with adaptive amplitude-frequency adjustment.

TABLE III
VERIFICATION OF THE ESTIMATED PARAMETERS

Method	R_{sopen} (Ω)	R_{error} (%)	L_{α_app} (mH)	L_{α_error} (%)	search time(s)
instrument measure	0.554	-	1.932	-	-
Tradition [21]	0.593	7.04	2.203	14.03	-
Proposed	0.581	4.87	2.06	6.62	0.68
[11]	0.583	5.23	2.118	8.8	1.82
[13]	0.5825	5.14	2.123	9.0	4.83

By pre-evaluating the system state and modifying the excitation frequency accordingly, the strategy still achieves rapid convergence to the target current without violating hardware limits.

Table III presents a comparative analysis of the identification results obtained using the proposed strategy and various open-loop algorithms, benchmarked against high-precision instrument measurements. The proposed scheme achieves comparable or superior accuracy relative to several state-of-the-art open-loop algorithms while requiring significantly fewer search steps due to the exponential iteration and safety-prediction mechanism. The identified parameters in this stage serve a critical dual purpose: they provide a sufficiently accurate baseline for initial controller autotuning and act as reference benchmarks for validating the subsequent closed-loop identification results.

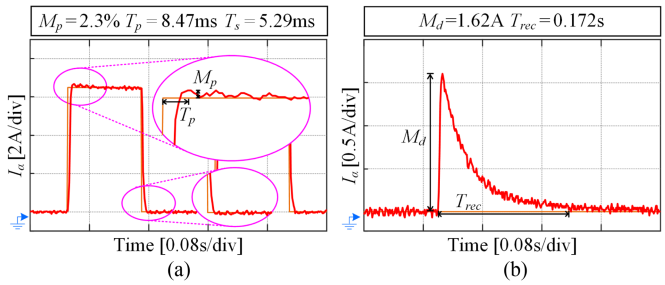

Fig. 11. Time-domain performance of the α-axis current. (a) Tracking. (b) Anti-interference.

B. Autotuned Current Loop: Optimal Damping Ratio

To validate the effectiveness of the motor parameters (R_α, $L_{\alpha\mathrm{app}}$) identified in the Section V-A and their utility in enabling fundamental current-loop control functionality, this section presents the dynamic performance of an automatically tuned proportional-integral (PI) current controller based on these parameters. Following the controller design methodology based on the optimal damping ratio, as outlined in Section III-C, the control algorithm automatically calculated the proportional gain and integral time constant. Fig. 11 illustrates the tracking performance of the autotuned current loop. Fig. 11(a) on the left depicts the d-axis current response to a step reference command. The system responds rapidly, achieving a settling time of approximately 1 ms with negligible overshoot or oscillation, demonstrating the controller's good stability and fast dynamic response capability based on the identified parameters. Fig. 11(b) on the right evaluates disturbance rejection by applying a step disturbance equivalent to 0.5 per unit of the rated voltage during steady-state operation. The current waveform effectively recovers its state, indicating the satisfactory robustness of the tuned system.

These experimental results demonstrate that the parameters identified through the proposed open-loop adaptive injection method can be effectively utilized for the fundamental tuning of the current controller. This enables stable current-loop control with the expected dynamic performance, paving the way for subsequent closed-loop identification procedures and normal operation of the drive system.

C. Closed-Loop Resistance Identification and Inverter Nonlinearity Compensation

After the current controller has been initialized using the apparent parameters obtained from the open-loop stage, the second stage of the framework carries out closed-loop identification to refine the stator resistance and quantify the inverter nonlinearity. As derived in Section IV-A, a single ramp-injection sequence enables simultaneous extraction of the stator resistance and the inverter voltage-error model parameters, avoiding the need for additional excitation procedures.

During the current ramp to its target value, the nonlinear voltage deviation $\Delta u_{d\mathrm{err}}$ is continuously monitored. As illustrated in the blue area of Fig. 9, $\Delta u_{d\mathrm{err}}$ exhibits a nonlinear

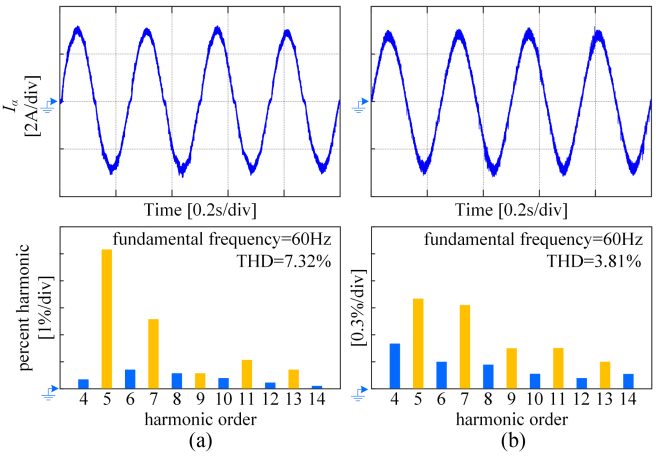

Fig. 12. Phase current waveform and THD analysis under 60 r/min, 1 N·m. (a) Without voltage compensation. (b) With voltage compensation.

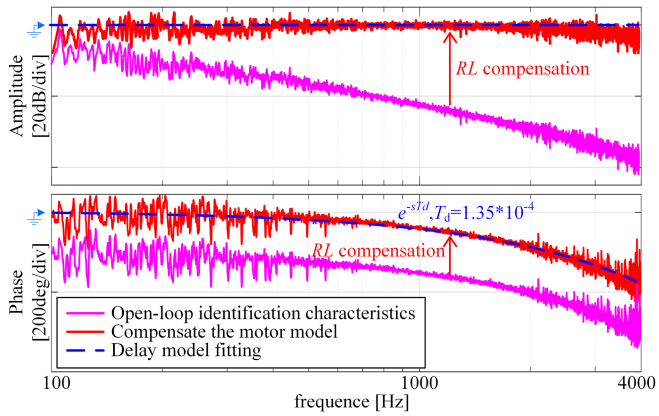

Fig. 13. Bode diagram of delay effect characteristics.

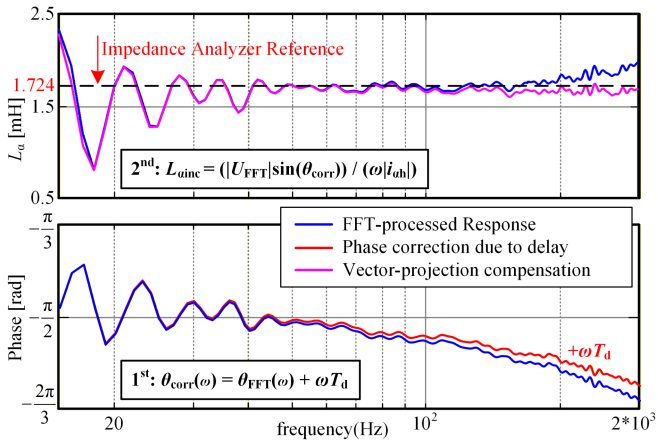

Fig. 14. Inductance identification under skin-effect compensation.

dependence on the *d*-axis current at low amplitudes but gradually approaches a linear relationship as the current increases. To achieve effective parameter decoupling, only the high-current linear segment is fitted: the slope yields the stator resistance estimate, and the intercept corresponds to $4/3*\Delta U$. Based on these quantities and the relationship derived in (25), the inverter nonlinearity parameter k is subsequently computed and applied for voltage-error compensation in the current loop.

A key feature of the proposed approach is that the stator resistance is inherently identified in three sequential stages throughout the full framework. They are the open-loop phase ($R_{sopen} = 0.581\ \Omega$), the initial closed-loop phase prior to inverter nonlinearity compensation ($R_s' = 0.5793\ \Omega$), and the final stage after compensation ($R_{sfinal} = 0.5764\ \Omega$). Since the closed-loop stages share identical current trajectories under the same ramp excitation, their difference arises solely from the treatment of the voltage. The fact that R_s' is obtained in the high-current saturation region explains its close proximity to R_{sfinal}, and the remaining small reduction after compensation confirms the validity of the derived inverter model.

The effectiveness of the combined identification-and-compensation procedure is further demonstrated through waveform and total harmonic distortion (THD) analysis. Under a 60 r/min and 1 N·m operating condition, the compensated current waveform becomes more symmetric and exhibits significantly suppressed HF harmonics, as shown in Fig. 12. Quantitatively, the THD is reduced by 47.9%, from 7.32% to 3.81%. Meanwhile, the identified final resistance shows only a 4.1% deviation from the reference value, and the entire closed-loop identification and compensation process completes within 2.1 s.

These results demonstrate that the proposed ramp-based closed-loop identification procedure can accurately estimate *Rs* and the inverter nonlinearity model, and that the resulting compensation substantially improves the quality of the current waveform. This validates the practicality of the closed-loop stage for self-commissioning applications and provides a reliable foundation for the subsequent inductance identification under magnetic saturation.

D. Identification of Incremental Inductance With Skin-Effect Compensation

As analyzed in Section IV-B, the HF skin effect and system delay collectively distort the voltage–current relationship, which can result in a systematic overestimation of the incremental inductance if not adequately compensated. Therefore, a two-stage compensation approach based on the delay identification and vector-projection-based compensation was proposed. This section evaluates the resulting improvement in incremental inductance-identification accuracy under magnetic saturation.

After the current reaches the rated maximum value, the total system delay is first quantified through a streamlined chirp-based procedure. A broadband chirp signal (up to $f_s/2$) is superimposed on the dc-biased current to excite the frequency response of the closed-loop current-controlled system. By applying FFT and linearly fitting the HF phase lag, as described in (35), a total delay of $T_d = 1.35*10^{-4}$ s is obtained, as illustrated in Fig. 13. This delay estimate is then used to compensate phase distortion and enable the accurate HF inductance extraction.

To quantify the impact of skin effect on incremental inductance under magnetic saturation, a low-to-medium-frequency chirp sweep (up to 2 kHz) is further superimposed on dc-biased current. The blue curve in Fig. 14 depicts the frequency-domain

TABLE IV
COMPARISON OF INDUCTANCE-IDENTIFICATION RESULTS

	Instrument Measure	Tradition Identification	Skin Effect Compensation
$L_{\alpha app}$(mH)	1.724	1.925	1.651
$L_{\alpha error}$(%)	-	11.65%	4.42%

response derived from FFT processing of the time-domain data. Due to transient response and frequency-dependent skin effect, the phase progressively deviates from the ideal $-90°$ quadrature relationship. Considering the necessity of observing phase information for skin-effect evaluation, as discussed in Section IV-B, the delay characteristics are compensated using (38) based on the FFT results, yielding the corrected phase (red curve in Fig. 14). The residual phase error exhibits characteristics attributable to skin effect.

Subsequently, the proposed vector-projection compensation is applied. Using the delay-corrected phase, the voltage phasor is decomposed into components parallel and orthogonal to the current. The orthogonal component, obtained according to (37), corresponds to the purely inductive voltage drop, from which the incremental inductance is computed. The resulting skin-effect-corrected inductance is plotted as the pink curve in Fig. 14. For comparison, dc-biased impedance analyzer measurements are included as the red dashed reference. The uncompensated identification exhibits a noticeable overestimation of $L_{\alpha \mathrm{inc}}$ at higher frequencies, whereas the proposed delay-decoupled and vector-projection-corrected results closely track the reference curve across the entire tested range. Table IV summarizes the quantitative comparison. The traditional method exhibits an inductance-identification error of 11.65%, while the proposed compensation reduces this error to 4.42%. These results confirm that the combined delay decoupling and vector-projection strategy effectively suppresses skin-effect-induced errors and enables high-precision incremental inductance identification in the saturated region.

Throughout the parameter identification process, apparent inductance is identified during the open-loop stage ($L_{\alpha \mathrm{app}} = 2.06$ mH), whereas incremental inductance is determined in the closed-loop stage following nonlinearity compensation ($L_{\alpha \mathrm{inc}} = 1.651$ mH). It is noteworthy that both parameters were identified under the motor's rated current condition, ensuring a consistent operating point for comparison. The fact that the identified incremental inductance is lower than the apparent inductance corroborates the expected influence of magnetic saturation at high current levels and further validates the accuracy of the identification methodology.

VI. CONCLUSION

As the beginning of the self-commissioning process, parameter identification must prioritize safety, efficiency, minimal initialization requirements, and universality. This article proposes a hybrid open/closed-loop identification strategy for PMSMs that explicitly compensates critical nonlinearities, including phase errors, inverter nonlinearity, and skin effects. By integrating excitation-adaptive amplitude–frequency open-loop injection with high-precision closed-loop magnetic saturation compensation and explicitly using minimum identified parameters as safe design references, the method achieves accurate and efficient parameter identification without manual intervention while guaranteeing operational safety. The experimental results validate the framework's effectiveness in enhancing self-commissioning performance, demonstrating improved accuracy, efficiency, and adaptability across diverse operating conditions.

While this work focuses exclusively on offline identification for self-commissioning, the acquired parameters facilitate advanced control strategies. Future work will extend this framework to online adaptive control and multimotor synchronization applications.

REFERENCES

[1] Z.-H. Liu, H.-L. Wei, X.-H. Li, K. Liu, and Q.-C. Zhong, "Global identification of electrical and mechanical parameters in PMSM drive based on dynamic self-learning PSO," *IEEE Trans. Power Electron.*, vol. 33, no. 12, pp. 10858–10871, Dec. 2018.

[2] G. Wang, R. Yang, and D. Xu, "DSP-based control of sensorless IPMSM drives for wide-speed-range operation," *IEEE Trans. Ind. Electron.*, vol. 60, no. 2, pp. 720–727, Feb. 2013.

[3] K. Liu, J. Feng, S. Guo, L. Xiao, and Z.-Q. Zhu, "Identification of flux linkage map of permanent magnet synchronous machines under uncertain circuit resistance and inverter nonlinearity," *IEEE Trans. Ind. Inform.*, vol. 14, no. 2, pp. 556–568, Feb. 2018.

[4] C. Gong, Y. Hu, J. Gao, Y. Wang, and L. Yan, "An improved delay-suppressed sliding-mode observer for sensorless vector-controlled PMSM," *IEEE Trans. Ind. Electron.*, vol. 67, no. 7, pp. 5913–5923, Jul. 2020.

[5] S. Rubino, O. Dordevic, R. Bojoi, and E. Levi, "Modular vector control of multi-three-phase permanent magnet synchronous motors," *IEEE Trans. Ind. Electron.*, vol. 68, no. 10, pp. 9136–9147, Oct. 2021.

[6] X. Wang, Z. Wang, Z. Xu, M. Cheng, W. Wang, and Y. Hu, "Comprehensive diagnosis and tolerance strategies for electrical faults and sensor faults in dual three-phase PMSM drives," *IEEE Trans. Power Electron.*, vol. 34, no. 7, pp. 6669–6684, Jul. 2019.

[7] S. Nadarajan, S. K. Panda, B. Bhangu, and A. K. Gupta, "Online model-based condition monitoring for brushless wound-field synchronous generator to detect and diagnose stator windings turn-to-turn shorts using extended Kalman filter," *IEEE Trans. Ind. Electron.*, vol. 63, no. 5, pp. 3228–3241, May 2016.

[8] Q. Wang, G. Wang, N. Zhao, G. Zhang, Q. Cui, and D. Xu, "An impedance model-based multiparameter identification method of PMSM for both offline and online conditions," *IEEE Trans. Power Electron.*, vol. 36, no. 1, pp. 727–738, Jan. 2021.

[9] S. A. Odhano, R. Bojoi, M. Popescu, and A. Tenconi, "Parameter identification and self-commissioning of AC permanent magnet machines—A review," in *Proc. Workshop Electron. Mach. Des., Control Diagnosis*, 2015, pp. 195–203.

[10] S. A. Odhano, P. Pescetto, H. A. A. Awan, M. Hinkkanen, G. Pellegrino, and R. Bojoi, "Parameter identification and self-commissioning in AC motor drives: A technology status review," *IEEE Trans. Power Electron.*, vol. 34, no. 4, pp. 3603–3614, Apr. 2019.

[11] J. Long, M. Yang, Y. Chen, D. Xu, and F. Blaabjerg, "A novel voltage injection based offline parameters identification for current controller auto tuning in SPMSM drives," *Energies*, vol. 13, 2020, Art. no. 3010.

[12] F. Erturk and B. Akin, "Spatial inductance estimation for current loop auto-tuning in IPMSM self-commissioning," *IEEE Trans. Ind. Electron.*, vol. 67, no. 5, pp. 3911–3920, May 2020.

[13] Q. Wang, G. Zhang, G. Wang, C. Li, and D. Xu, "Offline parameter self-learning method for general-purpose PMSM drives with estimation error compensation," *IEEE Trans. Power Electron.*, vol. 34, no. 11, pp. 11103–11115, Nov. 2019.

[14] D. Pengcheng, X. Dianguo, W. Bo, and Y. Yong, "Offline parameter identification strategy of permanent magnet synchronous motor considering the inverter nonlinearities," in *Proc. Int. Conf. Electron. Mach. Syst.*, 2022, pp. 1–5.

[15] S. A. Odhano, P. Giangrande, R. I. Bojoi, and C. Gerada, "Self-commissioning of interior permanent-magnet synchronous motor drives with high-frequency current injection," *IEEE Trans. Ind. Appl.*, vol. 50, no. 5, pp. 3295–3303, Sep./Oct. 2014.

[16] G. Wang et al., "Self-commissioning of permanent magnet synchronous machine drives at standstill considering inverter nonlinearities," *IEEE Trans. Power Electron.*, vol. 29, no. 12, pp. 6615–6627, Dec. 2014.
[17] N. Nomura and S. Higuchi, "Auto-tuning method of inductances for permanent magnet synchronous motors," in *Proc. Int. Power Electron. Conf.*, 2014, pp. 1522–1528.
[18] S. A. Odhano, R. Bojoi, Ş. G. Roşu, and A. Tenconi, "Identification of the magnetic model of permanent-magnet synchronous machines using DC-biased low-frequency AC signal injection," *IEEE Trans. Ind. Appl.*, vol. 51, no. 4, pp. 3208–3215, Jul./Aug. 2015.
[19] J.-S. Yoon, K.-G. Lee, J.-S. Lee, and K.-B. Lee, "Off-line parameter identification of permanent magnet synchronous motor using a Goertzel algorithm," *J. Elect. Eng. Technol.*, vol. 10, no. 6, pp. 2262–2270, Nov. 2015.
[20] Q. Wang et al., "An offline parameter self-learning method considering inverter nonlinearity with zero-axis voltage," *IEEE Trans. Power Electron.*, vol. 36, no. 12, pp. 14098–14109, Dec. 2021.
[21] P. Pescetto and G. Pellegrino, "Automatic tuning for sensorless commissioning of synchronous reluctance machines augmented with high-frequency voltage injection," *IEEE Trans. Ind. Appl.*, vol. 54, no. 5, pp. 4485–4493, Sep./Oct. 2018.
[22] P. Mattavelli, L. Tubiana, and M. Zigliotto, "Simple control autotuning for PMSM drives based on feedback relay," in *Proc. Eur. Conf. Power Electron. Appl.*, 2005, pp. 1–10.
[23] C. C. Hang, K. J. Astrom, and W. K. Ho, "Refinements of the Ziegler-Nichols tuning formula," *Proc. IEEE*, vol. 138, pp. 111–118, 1999.
[24] L. M. Gong and Z. Q. Zhu, "A novel method for compensating inverter nonlinearity effects in carrier signal injection-based sensorless control from positive-sequence carrier current distortion," *IEEE Trans. Ind. Appl.*, vol. 47, no. 3, pp. 1283–1292, May/Jun. 2011.
[25] J.-W. Chin, K.-S. Cha, J.-C. Park, D.-M. Kim, J.-P. Hong, and M.-S. Lim, "Investigation of AC resistance on winding conductors in slot according to strands configuration," *IEEE Trans. Ind. Appl.*, vol. 57, no. 1, pp. 316–326, Jan./Feb. 2021.
[26] D. Lin, P. Zhou, and Z. Zhang, "Reduced order modeling and parameter identification of induction motors based on FEA solutions," *IEEE Trans. Energy Convers.*, vol. 38, no. 2, pp. 1108–1117, Jun. 2023.
[27] A. G. Yepes, A. Vidal, J. Malvar, O. López, and J. Doval-Gandoy, "Tuning method aimed at optimized settling time and overshoot for synchronous proportional-integral current control in electric machine," *IEEE Trans. Power Electron.*, vol. 29, no. 6, pp. 3041–3054, Jun. 2014.
[28] D. G. Holmes, B. P. McGrath, and S. G. Parker, "Current regulation strategies for vector-controlled induction motor drives," *IEEE Trans. Ind. Electron.*, vol. 59, no. 10, pp. 3680–3689, Oct. 2012.
[29] D. G. Holmes, T. A. Lipo, B. McGrath, and W. Kong, "Optimized design of stationary frame three phase AC current regulators," *IEEE Trans. Power Electron.*, vol. 24, no. 11, pp. 2417–2426, Nov. 2009.
[30] K. Shao, J. Zheng, H. Wang, X. Wang, and B. Liang, "Leakage-type adaptive state and disturbance observers for uncertain nonlinear systems," *Nonlinear Dyn.*, vol. 105, no. 2, pp. 2299–2311, Jul. 2021.
[31] M. Zhu, C. Huang, S. Song, Y. Zhao, J. Qi, and D. Gong, "Adaptive vision-admittance-based leakage-type sliding mode control for uncertain collaborative robot with actuator saturation," *IEEE Trans. Syst., Man, Cybern., Syst.*, vol. 55, no. 11, pp. 8412–8423, Nov. 2025.

Junyu Zhao received the B.S. degree in electrical engineering in 2020 from Northwestern Polytechnical University, Xi'an, China, where he is currently working toward the Ph.D. degree in power electronics and electrical drives with the School of Electrical Engineering and Automation. His current research interests include servo systems, motor parameter identification, and control parameter self-tuning strategy.

Jun Gu received the B.S. degree in electrical engineering from Northwestern Polytechnical University, Xi'an, China, in 2024. He is currently working toward the M.S. degree in power electronics and electrical drives with the School of Electrical Engineering and Automation, Harbin Institute of Technology, Harbin, China. His current research interests include motor-drive control and motor parameter identification.

Yuting Wu (Student Member, IEEE) received the B.S. degree in electrical engineering from Huaqiao University, Xiamen, China, in 2022. She is currently working toward the M.S. degree in power electronics and electrical drives with the School of Electrical Engineering and Automation, Harbin Institute of Technology, Harbin, China. Her current research interests include the parameter identification of asymmetric motors in debugging free servo systems.

Dianguo Xu (Fellow, IEEE) received the B.S. degree in control engineering from Harbin Engineering University, Harbin, China, in 1982, and the M.S. and Ph.D. degrees in electrical engineering from the Harbin Institute of Technology (HIT), Harbin, China, in 1984 and 1989, respectively. In 1984, he joined as an Assistant Professor with the Department of Electrical Engineering, HIT, where he has been a Professor since 1994. From 2000 to 2010, he was the Dean of the School of Electrical Engineering and Automation, HIT, where he is currently the Vice President. His research interests include renewable energy generation, power quality mitigation, sensorless motor drives, and high-performance servo systems. Dr. Xu is an Associate Editor for IEEE TRANSACTIONS ON INDUSTRIAL ELECTRONICS.